TECHNICAL PAPER

Design, fabrication, and evaluation of functionally graded triply periodic minimal surface structures fabricated by 3D printing

Ibrahim M. Hassan[1] · Tawakol A. Enab[1] · Noha Fouda[1] · Ibrahim Eldesouky[1]

Abstract

Cellular structures are a favorite selection for the design of lightweight components and energy absorption applications due to several advantages such as their customizable stiffness and strength. In this investigation, functionally graded (FG) triply periodic minimal surfaces, Schoen-IWP (SIWP), and Schwarz primitive (SPrim) cellular structures were fabricated by masked stereolithography (MSLA) technique using ABS-like gray resin. The sample morphology, deformation behavior, mechanical characteristics, and energy absorption of graded and uniform structures were studied using experimental compression tests. The FG sample structures exhibited layer-by-layer collapse delaying shear failure. On the other hand, uniform samples showed complete diagonal shear failure. The total energy absorption to the densification point was 0.52 MJ/m^3 and 0.58 MJ/m^3 for graded and uniform SIWP, respectively. Additionally, the absorbed energy of the graded SPrim structure was 0.59 MJ/m^3 while the uniform one absorbed 0.27 MJ/m^3. The investigations showed that the graded SPrim absorbed more energy with high densification strain during the compression test.

1 Introduction

Cellular structures are considered multifunctional materials, providing several advantages in applications including heat exchangers [1, 2], biomedical scaffolds[3–6], lightweight structures, and energy absorption applications [7]. Traditional production methods of porous structures include chemical vapor deposition, physical vapor deposition, plasma spraying, investment casting [8], and powder

---

✉ Tawakol A. Enab
tenab@mans.edu.eg

Ibrahim M. Hassan
igarabie@mans.edu.eg

Noha Fouda
nfouda@mans.edu.eg

Ibrahim Eldesouky
ibrahim.eldesouky@mans.edu.eg

1 Production Engineering and Mechanical Design Department, Faculty of Engineering, Mansoura University, P.O. 35516, Mansoura, Egypt

---

metallurgy [9]. However, porous structures with controlled internal architectures and volume fractions are still difficult to fabricate through traditional fabrication methods.

Additive manufacturing (AM) presents a wide range of techniques that manufacture parts from CAD models as successive bonded layers. AM techniques provide more design freedom compared to conventional manufacturing methods, providing the ability to create complex lightweight parts with increased functionality. A new trend in the design of AM components is to replace solid volumes with lightweight cellular structures for several advantages such as improving energy consumption efficiency and improving material utilization [10–16]. Gibson and Ashby [17] showed that the mechanical performance of cellular structures is strongly related to their volume fraction. Cellular structures with graded variation in volume fraction, namely functionally graded (FG) cellular structures, are attracting more interest because of their customizable mechanical properties, suitability for bone ingrowth, and tissue engineering applications. Previous research focused on studying many FG structures, such as body-centered cube (BCC) [18], cubic [19], and diamond [20]. For example, Choy et al. [16] studied the mechanical performance and energy absorption behavior

for both cubic and honeycomb structures with variation in density and strut diameter, and they found that the energy absorption behavior of the graded structures was improved because of the distinctive features of layer-by-layer deformation. Maskery et al. [18] fabricated graded BCC cellular structures by selective laser melting (SLM) and showed that the energy absorbed by FG lattice structures was more than the uniform ones. Additionally, cell proliferation experiments revealed that FG octet truss and tetrahedron structures were more acceptable for bone tissue implantation than uniform structures due to their high cell proliferation rate [21]. However, conventional strut-type lattice structures turned out to cause more stress concentration near the nodes during loading which resulted in a weak mechanical performance [22, 23].

Currently, triply periodic minimal surfaces (TPMS) are investigated for designing FG cellular structures. TPMS are mathematically defined three-dimensional structures. TPMS structures are a promising solution that can be used to fabricate multifunctional materials for many applications. TPMS are smooth, infinitely extending, with large surfaces areas and zero mean curvatures [24–29]. Because of such favorable characteristics, TPMS cellular were used in biomedical applications such as tissue engineering scaffolds [30–32]. The TPMS family includes different types of structures. Examples include Schwarz primitive (SPrim), Schoen gyroid, Schoen I-graph and wrapped package-graph (SIWP), Neovius, Diamond, and Fischer–Koch S [33, 34]. Maskery et al. [35] examined the mechanical properties of three structures: gyroid, diamond, and primitive with the same relative density and found that primitive structures exhibited higher elastic modulus than the other two. The primitive structure exhibited strut stretching and buckling, while the bending-dominated deformation mode was observed in gyroid and diamond structures.

In addition to metallic and ceramic TPMS structures, researchers investigated 3D-printed polymer cellular TPMS structures [31, 36–39]. Al-Ketan et al. [40] compared the compressive mechanical performance of printed polymeric TPMS strut micro-lattice against sheet micro-lattice experimentally. They found that TPMS sheet-based structures showed better mechanical performance compared with strut micro-lattice since their mechanical performance is less affected by density variation. In another study, Zhang et al. [41] investigated the mechanical performance and energy absorption of three structures gyroid, diamond, and primitive that were printed of 316L stainless steels using SLM technique. The results showed superior mechanical properties compared to the BCC cellular structure which was related to a more stable failure mechanism and smooth structure geometry. Moreover, Zhao et al. [23] experimentally compared the mechanical properties and energy absorption between gyroid and primitive FG structures manufactured

by SLM from Ti–6Al–4 V powder. They found that the FG structures exhibited higher energy absorption than uniform structures. Lastly, Shixiang Yu et al. [42] fabricated uniform and graded TPMS structures using 3D printing and compared the yielding strength, plateau stresses, and energy absorption properties. The results showed that the graded primitive structure absorbed more energy while there was little difference between the energy absorption for both uniform and graded gyroid structures.

The research gap covered in the current study is investigating rarely studied sheet-based triply periodic minimal surfaces structures which are SIWP and SPrim structures. Moreover, most of literature focused on uniform structures instead of functionally graded structures and their suitability for engineering applications, such as energy absorption applications and lightweight designs.

This paper presents a comparative study of the mechanical performance of two different functionally graded cellular structures versus their uniform counterparts. SIWP and SPrim cellular structures were investigated. The samples were fabricated using the vat photopolymerization additive manufacturing technique. The tested samples were evaluated in terms of sample morphology, deformation behavior, and energy absorption.

2 Material and methods

2.1 Cellular design

SIWP and SPrim cellular structures with controlled volume fraction and number of unit cells can be generated by finding the iso-surface (U = 0) and treating these surfaces as the boundary between solid and void material phases of TPMS equations [39, 43] as.

$$
\begin{aligned}
U_{SIWP} = &\left(2\left(\cos\left(w_x X\right)\cos\left(w_y Y\right) + \cos\left(w_x X\right)\cos\left(w_z Z\right)\right.\right. \\
&\left.+ \cos\left(w_y Y\right)\cos\left(w_z Z\right)\right) - \left(\cos\left(2w_x X\right)\right. \\
&\left.\left.+ \cos\left(2w_y Y\right) + \cos\left(2w_z Z\right)\right)\right) - t
\end{aligned}
$$

(1)

$$
U_{SPrim} = \cos\left(w_x X\right) + \cos\left(w_y Y\right) + \cos\left(w_z Z\right) - t
$$

(2)

For each of the previous equations, w_i represent the TPMS function repetitions, expressed by $w_i = 2\pi\frac{n_i}{l_i}$ (where $i = x, y, z$), as n_i specify the number of cells repetitions and l_i determine the structure size in x, y, z directions, t is used to specify the volume fraction in the three directions.

For investigation of mechanical performance of the cellular structures. Two uniform (U) and two graded (G) structures were examined (G-SIWP, U-SIWP, G-SPrim, and U-SPrim). The cellular structures consisted of 5*5*5 cells

with a 5 mm cell size for each sample. The graded structures had relative density (the density of cellular structure to the density of solid material) varying linearly and continuously from 0.24 to 0.32 along the z-axis. The gradation in the strut thickness and the pore size of designed samples is illustrated in Fig. 1, with the vertical dimensions representing the strut thickness and the horizontal dimensions representing the pore size. The uniform samples were designed with a constant relative density of 0.28. These models were designed using FLATT PACKED software [44] that provides the ability to control the unit cell dimension and values of volume fraction. The total structure volume was 25*25*25 mm as shown in Fig. 2.

2.2 Model fabrication

The flowchart displayed in Fig. 3. describes the steps of modeling and the printing process. Sixteen cubic test samples were 3D printed using Masked Stereolithography (MSLA) technique. The machine used was Phrozen Shuffle XL 2019 (Phrozen, Hsinchu City, Taiwan). The machine employs a high pixel density LCD screen with resolution of 3845×2400 pixels, for X and Y directions assembled between an array of ultraviolet (UV) light emitting diodes (LEDs) and a transparent resin tank. The designed porous CAD models were first sliced into layers, then each layer was sequentially displayed as a mask on the screen. The UV light was projected through the mask to harden a layer of resin onto the build platform. At the beginning of the hardening process of the liquid resin, the build platform was at the bottom of the resin vat. After completing the first layer, the build platform was raised at a constant increment equal to the specified layer thickness which equals 50 μm till the full sample was 3D printed. ABS-like gray resin supplied by FEPshop (FEPshop, Groningen, Netherlands) was used for
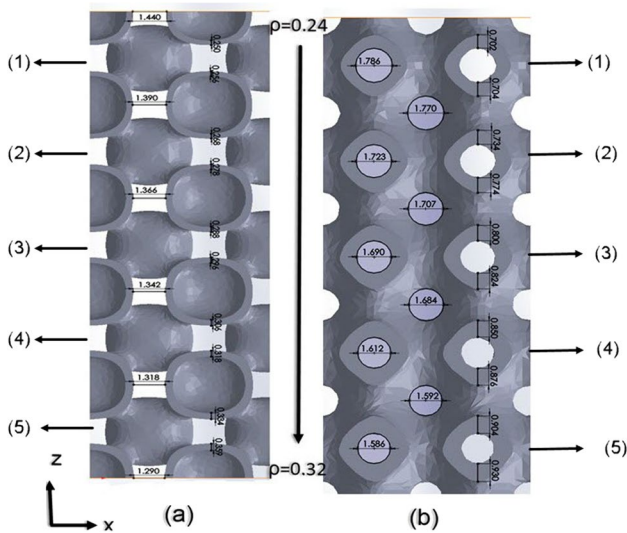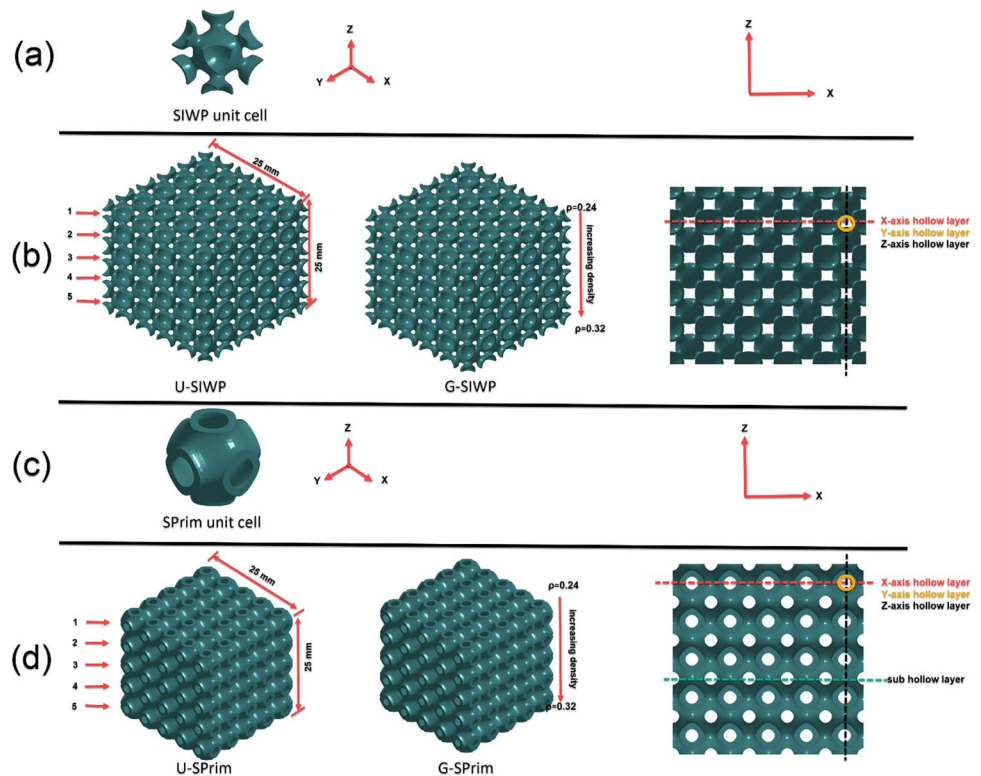

Fig. 1 The gradation in the dimensions of strut thickness and pore size of **a** G-SIWP structures, and **b** G-SPrim structures

Fig. 2 CAD Models representation **a** SIWP unit cell, **b** G-SIWP and U-SIWP structures, **c** SPrim unit cell, and **d** G-SPrim and U-SPrim structures
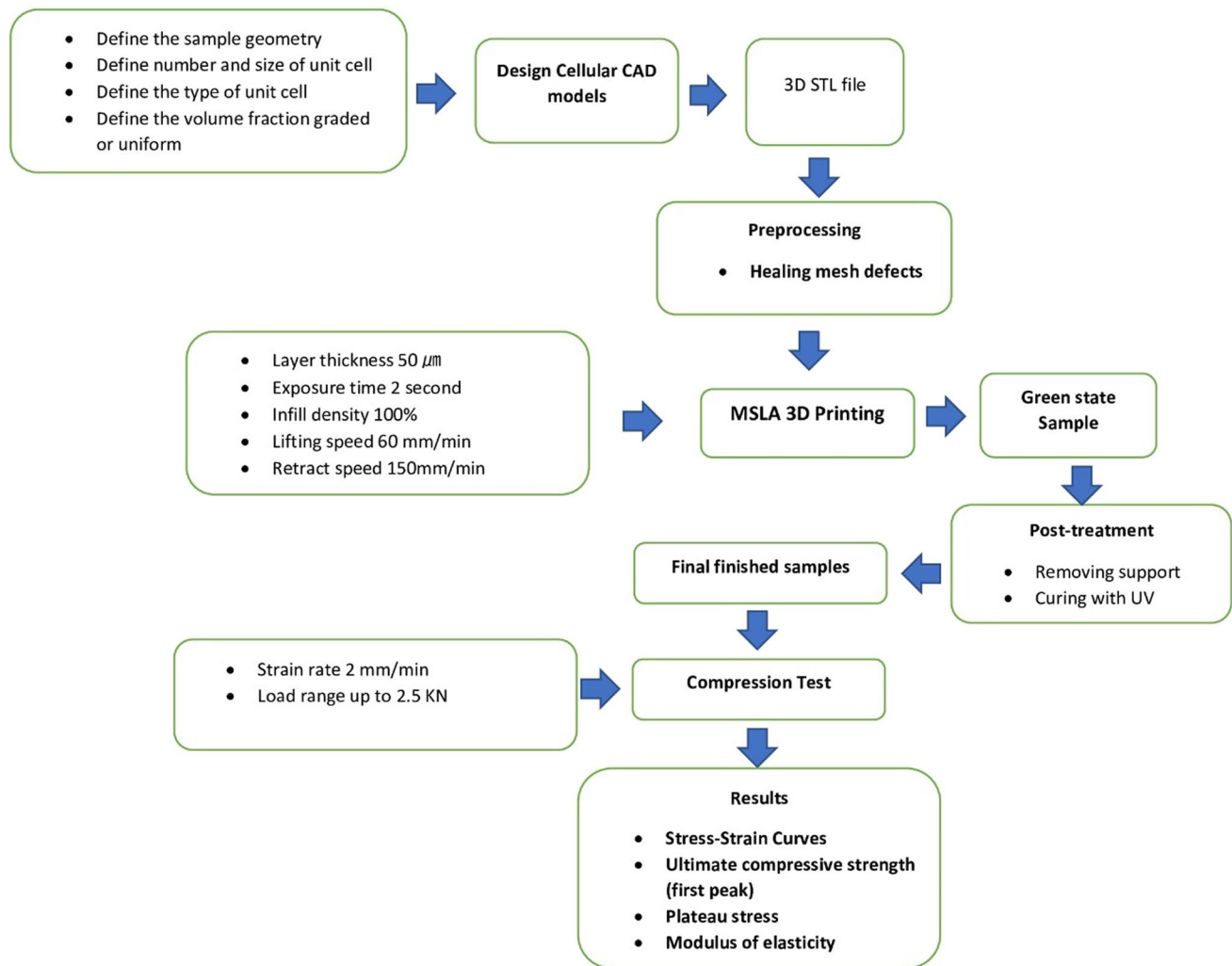
Fig. 3 Flowchart of the procedures of the current study

the samples 3D printing. The resin has a density of 1.10 g/cm³ and a tensile modulus of elasticity of 1.05 GPa [45] which is suitable for general modeling and industrial prototype proofing. Next, the printed samples were cleaned using ethyl alcohol at 70% concentration with a washing time of 3 min [46, 47]. The structures were built with external supports with cylindrical shape and conical connection that were removed manually by pliers. The supports were made of the same material used for building the samples (ABS-like gray resin). Later, the samples were post-cured for 60 s using a curing unit which is equipped by a rotating platform with 385 and 405 nm dual-band LED beads.

2.3 Characterization

Geometric dimensions of the MSLA samples were measured using a digital caliper with an accuracy of 0.01 mm. Six measurements of the wall thickness and pore size were

taken for each printed sample using a digital optical microscope at a magnification level of 100x (VHX-1000 digital microscope, Keyence, NJ, USA). The mass of all sample was measured by electronic balance with a resolution of 0.1 mg (Ohaus Adventurer, Parsippany, USA). The average mass of each type was calculated. A universal mechanical testing machine (Lloyd Materials Testing, AMETEK, USA) with a 2.5 kN load cell was used to perform uniaxial compression tests according to ASTM D695 [48] standard at a strain rate of 2 mm/min. A digital camera used in recording was 16MP with video resolution 1080p/30fps was positioned in front of the samples in order to record the deformation of the samples up to 70% strain. Mechanical testing of four cubes of each structure was performed. The normal stress (σ) was calculated by dividing the applied load by the bounding cross-sectional area of the specimen. The normal strain (ε) was evaluated by dividing displacement into the initial sample's height. Accordingly, the elastic modulus of samples was

calculated from the slope of the curve at the elastic region. The first maximum compressive stress was determined as the stress reached to first stress peak (yielding point) after the linear proportional limit. The plateau stress was evaluated as the arithmetical mean of stress between 20 and 40% compressive strain. Also, the densification strain was defined as the strain at which the tangent's slope equals that of the elastic region. The area under the curve up to 50% strain was computed to calculate energy absorption per unit volume.

3 Results and discussion

All samples were printed from the same material (ABS-like gray resin) with same printing parameters, and the samples were printed in batches. Accordingly, only the effect of the cell structure was evaluated.

3.1 Structure morphology

The MSLA prepared TPMS samples are shown in Fig. 4. All samples were produced with the MSLA technique with smooth surface quality. Visual inspection showed that FG samples had a continuous variation in thickness.

Measurements of the wall thickness and pore size were taken for each printed sample of SIWP and SPrim structures using a digital optical microscope as shown in Fig. 5. The dimensions of the wall thickness and pore size of the four structures are summarized in Table 1. The dimensions of printed samples were higher than designed models for all the structures which are in accordance with other studies [49, 50]. For G-SIWP and U-SIWP the average measured wall thickness had excellent conformity higher than 84 and 81%, respectively. Similarly, the average measured wall thickness was 94 and 96% for G-SPrim and U-SPrim, respectively, which were considered to have more accuracy than SIWP structures. The measured pores size of G-SIWP and U-SIWP structures had conformance with designed pores higher than 95 and 93%, respectively. Likewise, the SPrim structures were in good agreement with the designed pores with accuracy higher than 96 and 97% G-SPrim and U-SPrim, respectively.

Designed and actual mass of samples with the resulting relative error is summarized in Table 2. Samples exhibited a deviation in mass between the designed and the printed samples. SIWP samples showed a large deviation between the designed and actual printed samples with a relative error of 40 and 46% for G-SIWP and U-SIWP, respectively. On the other hand, the relative error of mass among the SPrim

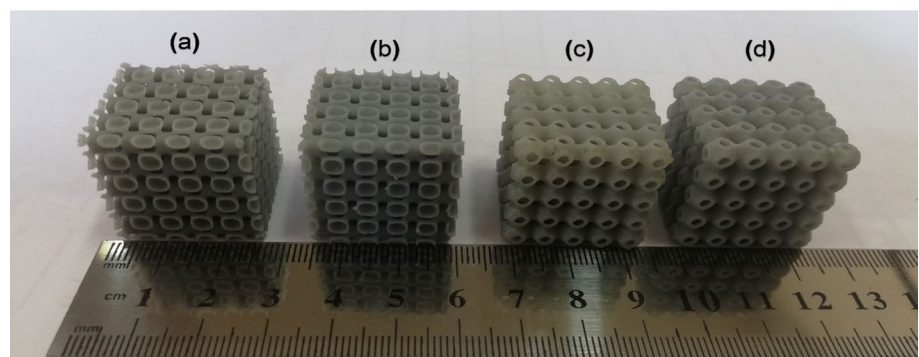**Fig. 4** The MSLA fabricated TPMS samples **a** G-SIWP, **b** U-SIWP, **c** G-SPrim, and **d** U-SPrim

Fig. 5 Strut thickness and pore size of one unit cell of **a** SIWP, **b** SPrim
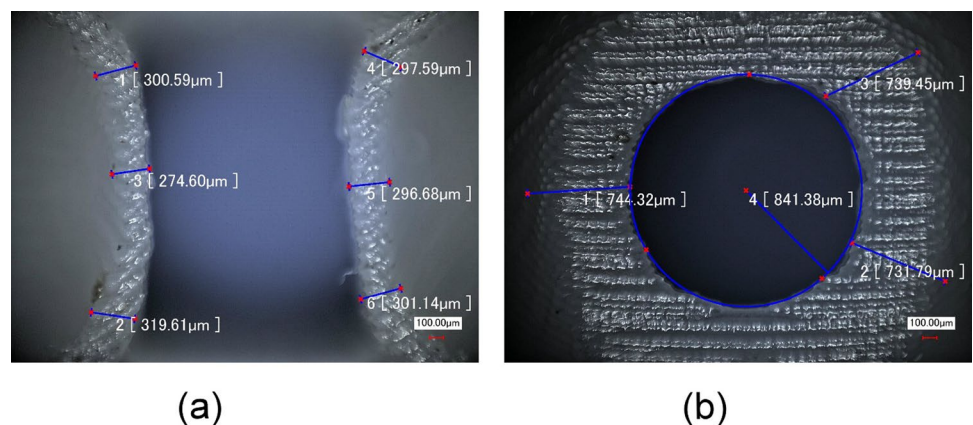
Table 1 Geometric characteristics of the different cellular samples

Sample type	Designed wall thickness (μm)	Measured wall thickness (μm)	Designed pore size (μm)	Measured pore size (μm)
G-SIWP	244–364	285 ± 26–392 ± 9	1294–1414	1243 ± 36–1379 ± 19
U-SIWP	290	347 ± 17	1358	1267 ± 45
G-SPrim	695–948	754 ± 31–933 ± 14	1539–1794	1491 ± 44–1746 ± 52
U-SPrim	802	835 ± 21	1692	1652 ± 30

Table 2 Designed versus measured mass of cellular structures

| Sample type	Designed mass (gram)	Measured mass (gram)	Relative error (%)
G-SIWP	4.908	6.9 ± 0.15	40.5
U-SIWP	4.803	6.7 ± 0.16	46.42
G-SPrim	4.804	5.2 ± 0.09	8.2
U-SPrim	4.767	5.1 ± 0.08	6.9

structures did not exceed 8.2 and 9.6% for graded and uniform SPrim structures, respectively. The SIWP samples showed increased mass compared to the design values. This deviation was related to the geometrical shape of the unit cell that is based on a sheet-type architecture which resulted in closed spherical volume that led to material entrapment. Similar results were obtained by Alketan et al. [51], who found that the deviation in mass increases with decreasing the relative density of the unit cell of the IWP structure.

3.2 Deformation behavior

Photographs representing the deformation of graded and uniform samples during compression test at different strain levels are collated in Fig. 6. For G-SIWP structures, the deformations began at the layer with the thinnest struts and cracks progressed row by row to the layer with the thickest struts. The clear sequential layers collapse was related to the increased cross-sectional area of the structure when the wall thickness is increased gradually. Failure started at 19% strain, then the structure visibly failed at nearly 37%. In contrast, U-SIWP samples showed diagonal shear band failure when the stress reached the first stress peak resulting in a significant reduction in stress and a limited capability to resist the applied force after the first collapse.

In the G-SPrim structures, the failure started from layers with low volume fractions then gradually extended to layers with high volume fractions in a sequential layer-by-layer manner similar to G-SIWP structures. The failure appeared at 11% strain with obvious layer collapses. On the other hand, the U-SPrim structures showed complete diagonal shear failure occurred at strain 17%. U-SIWP and U-SPrim had a similar deformation behavior to other uniform lattice structures such as the honeycomb structure [19], BCC structure [23], and diamond structure [52], where the maximum shear stress was at 45° to the direction of load [22]. This can be interpreted by the fact that they all have visible interconnected pores along the three orthogonal directions as shown in Fig. 1. This interconnectivity causes the structure to be vulnerable to fracture due to highly localized normal and

Fig. 6 Deformation behavior at different strain levels during compression testing of graded and uniform SIWP and SPrim structures
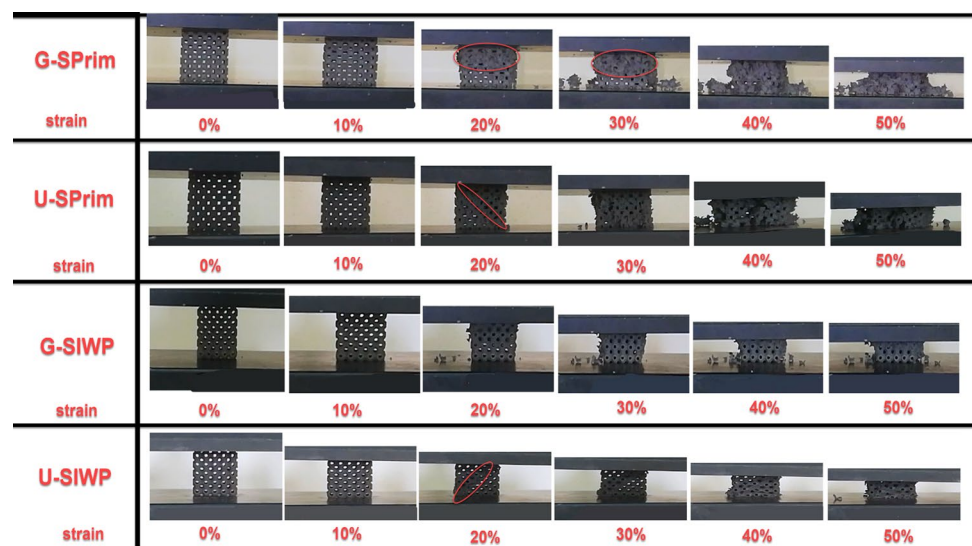
shear stress. It was also verified using numerical analysis in the previous literature [38, 41].

3.3 Mechanical behavior

The mechanical performance of graded and uniform SIWP and SPrim cellular samples during the compression test is shown in Fig. 7. There were three distinct regions, namely elastic, plastic, and densification regions. Clear stress peaks were noted for all samples structures as the first stress peak occurrence was followed by a notable reduction in stress level as presented in Fig. 7.

As shown in Fig. 7a. G-SIWP structure started to fail when it reached the yielding stress (first peak stress) of approximately 1.96 MPa, at a corresponding strain of 19% on average. It was also noted that a significant drop in the values of stress occurred followed by poor recovery. Next,

the G-SIWP specimens reached the densification stage, where the structures exhibited high compressive resistance due to the cell wall contact. The densification strain was approximately 61.83% while the average densification stress was 1.19 MPa for all samples.

For the U-SIWP structure, the plastic collapse began at a low strain level of 13% after the first peak stress of 1.945 MPa on average compared to G-SIWP started failure at high strain. Following that, U-SIWP reached densification at a stress of 0.926 MPa and strain of 69.37% as shown in Fig. 7b.

Failure started for the G-SPrim structures at low strain values of 11% strain after reaching a maximum strength equal to 1.039 MPa on average representing the first stress peak. Afterward, stress values showed a minor decrease and remained stable with little increase in the plateau region until the densification occurred. From the visual observation
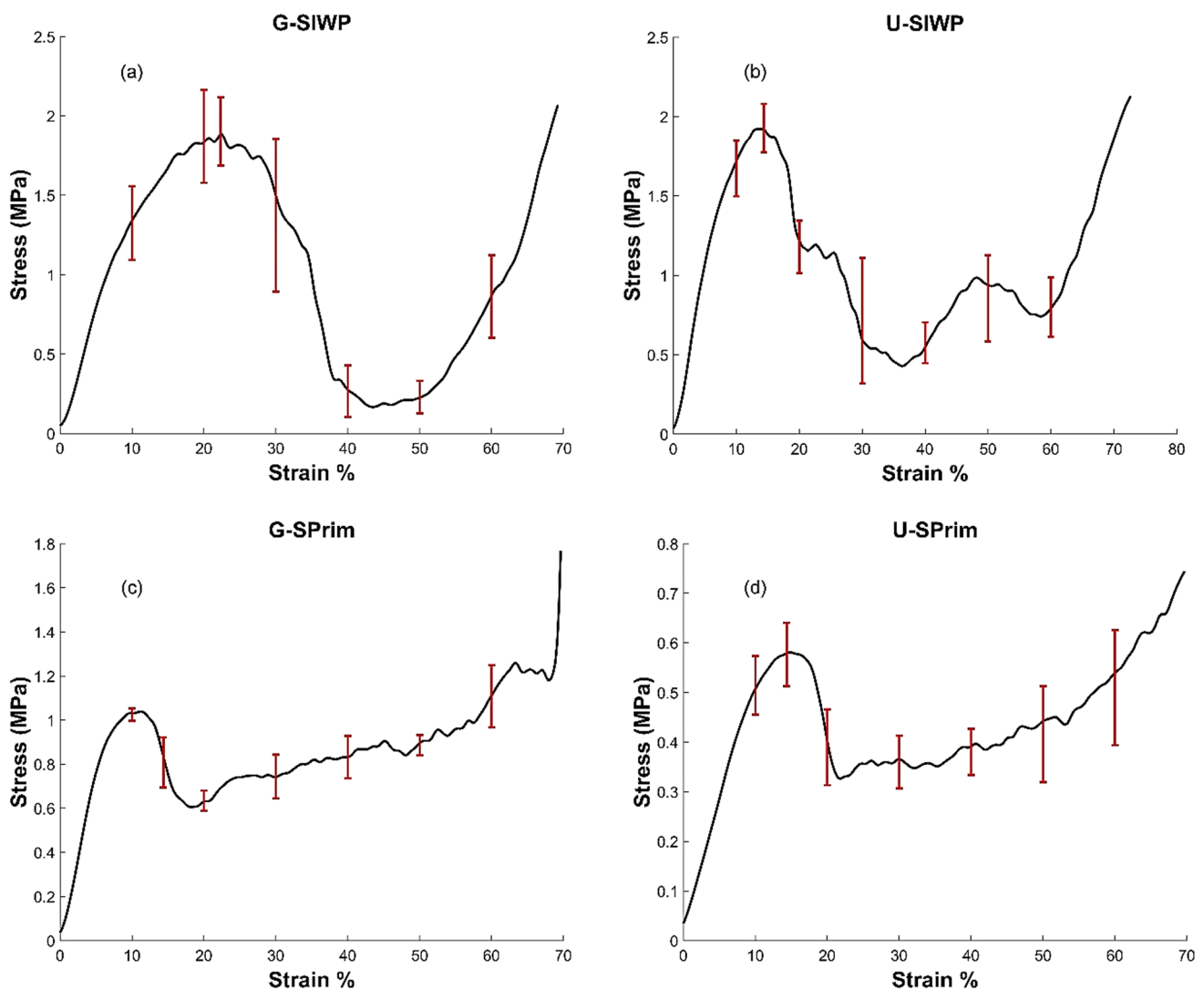

Fig. 7 The average stress–strain curves of **a** G-SIWP, **b** U-SIWP, **c** G-SPrim, and **d** U-SPrim based on three samples of each type

of the G-SPrim behavior, there was a long plateau region which is considered as an important factor in energy absorption applications. The densification strain was about 68.5% and the average stress was 1.19 MPa as shown in Fig. 7c. The U-SPrim structure had a similar trend in stress behavior as the G-SPrim but at lower stress values as presented in Fig. 7d. As the elastic region ended at strain 15% with 0.58 MPa average stress. Then the deformation ended with the start of densification at strain 63.78% and stress was 0.67 MPa.

The mechanical properties of SIWP and SPrim are summarized in Table 3. The first maximum compressive strength and the elastic modulus values of all graded samples were higher than the uniform ones Fig. 8, shows the combined graph of the stress–strain curve for one sample of each tested structure type. The SIWP samples showed higher mechanical performance than SPrim samples in both graded and uniform for the same volume fraction, which showed that the mechanical performance of cellular structures did not depend only on the variation of volume fraction but also depend on the unit cell designs. Another factor that affects the mechanical behavior is the deviation in mass as shown in Table 2. Accordingly, the relative density is directly affected by deviation in mass at a constant sample volume. The relative density is directly related to the mechanical performance of cellular materials in reference to following Gibson–Ashby relationship between the compressive stress and the relative density:

$$\frac{\sigma}{\sigma_0} = c \left(\frac{\rho}{\rho_0} \right)^n \tag{3}$$

where σ and ρ are the compressive stress and density of cellular structures, respectively. σ_0 and ρ_0 are the compressive stress and the density of the solid material. C is a constant related to the unit cell shape and the exponent n is a constant determined by the mechanical failure mode of the unit cell. For that reason, as the mass increases the compressive strength increases, which explains why the SIWP had the highest elastic modulus and compressive strength. The results of the current study are in good agreement with
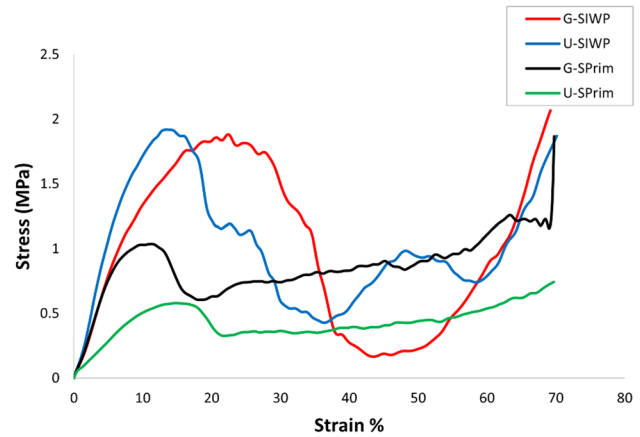

Fig. 8 Stress–strain curves of a representative sample for all tested designs

previous studies. For example, Abueidda et al. [38, 53] analyzed the mechanical performance of gyroid, SIWP, SPrim, and Neovius structures and reported that SIWP showed a higher elastic modulus and compressive stress than the SPrim structure. Additionally, Al-Ketan et al. [54] showed that the sheet SIWP structures exhibited higher mechanical properties than other tested structures.

It is important to relate the Young's modulus of specimen to the respective specimen's mass to overcome the problem of mass deviation in printed samples. Accordingly, a relative modulus of elasticity was calculated by dividing the cellular elastic modulus to the mass of samples as shown in Table 3. It is notable that SIWP structures exhibited a higher relative modulus than SPrim structures.

For demonstrating the relation between the deformation capacity of the original printing material and those observed in cellular structures, relative elasticity of cellular was calculated by dividing the cellular elastic modulus to modulus of solid material as shown in Table 3. The notable reduction in the elastic modulus of cellular structures could be useful for biomedical applications.

Table 3 Mechanical properties of printed samples

Sample	Modulus of elasticity (MPa)	First maximum compressive strength (MPa)	Plateau stress (MPa)	Relative modulus per mass (MPa/gram)	Relative elasticity $*10^{-3}$
G-SIWP	15.68 ± 4.1	1.964 ± 0.180	1.272 ± 0.235	2.272	14.93
U-SIWP	13.55 ± 1.94	1.945 ± 0.17	0.797 ± 0.092	2.022	12.90
G-SPrim	9.92 ± 0.95	1.0398 ± 0.004	0.759 ± 0.023	1.907	9.44
U-SPrim	5.179 ± 0.69	0.583 ± 0.066	1.079 ± 0.068	1.015	4.93

4 Energy absorption

One of the most common applications of cellular structures is energy absorption for impact protection, such as the design of protective and packaging devices. Studying cellular structures for energy absorption behavior gives a quantitative scale for comparing and choosing candidate cellular structures for energy absorption applications. Figure 9 presents the cumulative absorbed energy per unit volume, W_v, versus compressive strain for graded and uniform SIWP and SPrim structures. The difference in the absorbed energy between graded and uniform SIWP structures is not as significant as that of SPrim.

The total absorbed energy per unit volume to densification points and the energy absorption up to 50% strain for both graded and uniform cellular structures can be calculated by integrating stress and strain diagrams according to the following equation.

$$W_V = \int_0^\varepsilon \sigma(\varepsilon)d\varepsilon \tag{4}$$

where $\sigma(\varepsilon)$ represent stress (σ) related to strain (ε). The results are summarized in Table 4.

For SIWP structures, the total absorbed energy up to densification strain was 0.516 MJ/m^3 and 0.576 MJ/m^3 for graded and uniform, respectively. In SPrim structures, the
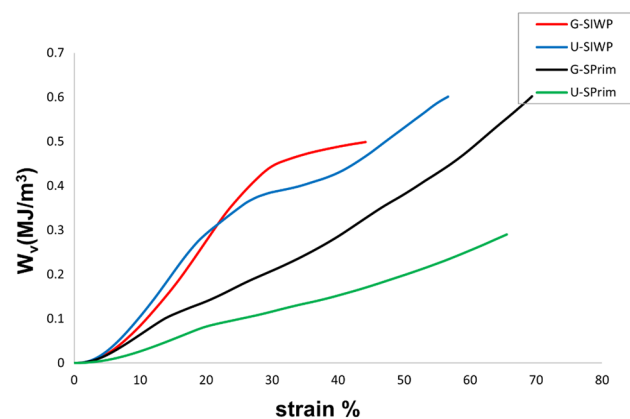
FG specimens had higher cumulative absorbed energy compared to uniform structures with large compressive strains. The total absorption energy of the G-SPrim structure at the densification point was 0.589 MJ/m^3 which is 2.197 times higher than the U-SPrim structure that absorbed 0.268 MJ/m^3 of energy at densification. According to the absorbed energy per unit volume (Wv) to densification point of the four structures under study, when comparing the G-SIWP structure to the U-SIWP structure, the structural toughness remains nearly unchanged however, when comparing the G-SPrim structure to the uniform one, the structural toughness changes significantly. For energy absorption up to strain 50% FG samples exhibited higher absorbed energy than the uniform samples.

To alleviate the effect of measured mass deviation of the printed samples from the target mass, energy absorption per mass, was calculated as shown in Table 4. The G-SIWP absorbed 1168 J/kg while the total energy absorption per unit mass equal 1343 J/Kg for uniform. It could be concluded that there was a little difference between graded and uniform SIWP. One the other hand, for SPrim structure, the total absorbed energy for unit mass was 1769 J/kg and 821 J/kg for both graded and uniform, respectively. Accordingly, the graded SPrim structure absorbed energy twice as the uniform one.

5 Conclusions

The present study focused on rarely studied sheet-based TPMS cellular structures. Sheet-based TPMS cellular structures showed improved performance compared to strut-type cellular structure as investigated previously in the literature. The mechanical performance of different FG TPMS cellular structures was studied under compressive testing. Samples were successfully 3D printed by MSLA technology using ABS-like gray Resin. Deformation behavior, mechanical performance, and energy absorption capacity of FG cellular samples were experimentally examined and compared to their uniform counterparts. The following conclusions were deduced:

1. The compression test showed that the deformation of FG cellular structure occurred gradually from the thinnest

Fig. 9 Cumulative energy absorption per unit volume (Wv) for graded and uniform SIWP and SPrim structures

Table 4 Total absorbed energy per unit volume (W_v) of the four structures under study

Sample	Densification strain (ε_d) %	Energy absorption up to densification strain (MJ/m^3)	Energy absorption up to 50% strain (MJ/m^3)	Energy absorption per unit mass (J/kg)
G-SIWP	45 ± 2.22	0.516 ± 0.04	0.525 ± 0.06	1168.478
U-SIWP	57 ± 3.10	0.576 ± 0.06	0.509 ± 0.026	1343.284
G-SPrim	68.54 ± 0.77	0.589 ± 0.02	0.385 ± 0.005	1769.832
U-SPrim	63.78 ± 4.45	0.268 ± 0.07	0.195 ± 0.03	821.0784

struts to the thickest struts in a sequential layer-by-layer manner. In contrast, uniform samples exhibited shear failure at plane oriented by 45° to the loading direction.

2. The compressive strength of G-SPrim structures increased by 80% than the uniform one. In general, the SIWP samples exhibited larger compressive stress and modulus of elasticity than SPrim in both graded and uniform.

3. The energy absorption of G-SIWP and U-SIWP structures at densification point presented a minor variation, exhibiting 0.516 and 0.576 MJ/m^3, respectively.

4. The total absorbed energy of the U-SPrim structure at densification points was only 54% of the G-SPrim capacity (0.589 MJ/m^3). In general, G-SPrim absorbed more energy than the other studied models.

The graded SPrim structure presented improved deformation behavior and energy absorption capacity compared to its uniform counterpart making it a promising candidate for impact application, lightweight design, and orthopedic implants.

Declarations

Conflict of interest The authors declared no potential conflicts of interest concerning the research, authorship, and publication of this article.

References

1. Rashed MG et al (2016) Metallic microlattice materials: a current state of the art on manufacturing, mechanical properties and applications. Mater Des 95:518–533

2. Catchpole-Smith S et al (2019) Thermal conductivity of TPMS lattice structures manufactured via laser powder bed fusion. Addit Manuf 30:100846

3. Ma S et al (2020) Manufacturability, mechanical properties, mass-transport properties and biocompatibility of triply periodic minimal surface (TPMS) porous scaffolds fabricated by selective laser melting. Mater Des 195:109034

4. Zhang X-Y et al (2020) Biomechanical influence of structural variation strategies on functionally graded scaffolds constructed with triply periodic minimal surface. Addit Manuf 32:101015

5. Eldesouky I et al (2017) Electron beam melted scaffolds for orthopedic applications. Addit Manuf 17:169–175

6. Li Z-H et al (2020) Mechanical properties of AlSi10Mg lattice structures fabricated by selective laser melting. Mater Des 192:108709

7. Mines RAW et al (2013) Drop weight impact behaviour of sandwich panels with metallic micro lattice cores. Int J Impact Eng 60:120–132

8. Brothers AH, Dunand DC (2008) Mechanical properties of a density-graded replicated aluminum foam. Mater Sci Eng A 489(1):439–443

9. Cherradi N, Kawasaki A, Gasik M (1994) Worldwide trends in functional gradient materials research and development. Compos Eng 4(8):883–894

10. Yan C et al (2015) Microstructure and mechanical properties of aluminium alloy cellular lattice structures manufactured by direct metal laser sintering. Mater Sci Eng A 628:238–246

11. Brackett DJ et al (2014) An error diffusion based method to generate functionally graded cellular structures. Comput Struct 138:102–111

12. Wei S et al (2021) Mechanical response of triply periodic minimal surface structures manufactured by selective laser melting with composite materials. Acta Metall Sin (Engl Lett) 35(3):397–410

13. Jam A et al (2022) Manufacturability of lattice structures fabricated by laser powder bed fusion: a novel biomedical application of the beta Ti–21S alloy. Addit Manuf 50:102556

14. Yang L et al (2018) Mechanical response of a triply periodic minimal surface cellular structures manufactured by selective laser melting. Int J Mech Sci 148:149–157

15. Kim WR et al (2020) Fabrication of porous pure titanium via selective laser melting under low-energy-density process conditions. Mater Des 195:109035

16. Wu YC et al (2018) Structural design and mechanical response of gradient porous Ti–6Al–4V fabricated by electron beam additive manufacturing. Mater Des 158:256–265

17. Gibson LJ (2003) Cellular solids. MRS Bull 28(4):270–274

18. Maskery I et al (2016) A mechanical property evaluation of graded density Al–Si10–Mg lattice structures manufactured by selective laser melting. Mater Sci Eng, A 670:264–274

19. Choy SY et al (2017) Compressive properties of functionally graded lattice structures manufactured by selective laser melting. Mater Des 131:112–120

20. Surmeneva MA et al (2017) Fabrication of multiple-layered gradient cellular metal scaffold via electron beam melting for segmental bone reconstruction. Mater Des 133:195–204

21. Wang Y et al (2018) Ternary hybrid PtM@polyaniline (M = Ni, FeNi) counter electrodes for dye-sensitized solar cells. Electrochim Acta 291:114–123

22. Qiu C et al (2015) Influence of processing conditions on strut structure and compressive properties of cellular lattice structures fabricated by selective laser melting. Mater Sci Eng A 628:188–197

23. Zhao M et al (2018) Improved mechanical properties and energy absorption of BCC lattice structures with triply periodic minimal surfaces fabricated by SLM. Materials 11(12):2411

24. Kapfer SC et al (2011) Minimal surface scaffold designs for tissue engineering. Biomaterials 32(29):6875–6882

25. Yang S-D, Lee HG, Kim J (2010) A phase-field approach for minimizing the area of triply periodic surfaces with volume constraint. Comput Phys Commun 181(6):1037–1046

26. Chen H-Y, Kwon Y, Thornton K (2009) Multifunctionality of three-dimensional self-assembled composite structure. Scr Mater 61(1):52–55

27. Jung Y, Torquato S (2005) Fluid permeabilities of triply periodic minimal surfaces. Phys Rev E 72(5):056319

28. Zhang L et al (2021) Hierarchical sheet triply periodic minimal surface lattices: design, geometric and mechanical performance. Mater Des 209:109931

29. Al-Ketan O, Lee DW, Abu Al-Rub RK (2021) Mechanical properties of additively-manufactured sheet-based gyroidal stochastic cellular materials. Addit Manuf 48:102418

30. Rajagopalan S, Robb RA (2006) Schwarz meets schwann: design and fabrication of biomorphic and durataxic tissue engineering scaffolds. Med Image Anal 10(5):693–712

31. Melchels FPW et al (2010) Mathematically defined tissue engineering scaffold architectures prepared by stereolithography. Biomaterials 31(27):6909–6916

32. Melchels FPW et al (2010) Effects of the architecture of tissue engineering scaffolds on cell seeding and culturing. Acta Biomater 6(11):4208–4217

33. Abueidda DW et al (2016) Effective conductivities and elastic moduli of novel foams with triply periodic minimal surfaces. Mech Mater 95:102–115

34. Abueidda DW, Jasiuk I, Sobh NA (2018) Acoustic band gaps and elastic stiffness of PMMA cellular solids based on triply periodic minimal surfaces. Mater Des 145:20–27

35. Maskery I et al (2018) Insights into the mechanical properties of several triply periodic minimal surface lattice structures made by polymer additive manufacturing. Polymer 152:62–71

36. Li D et al (2018) Optimal design and modeling of gyroid-based functionally graded cellular structures for additive manufacturing. Comput Aided Des 104:87–99

37. Afshar M et al (2016) Additive manufacturing and mechanical characterization of graded porosity scaffolds designed based on triply periodic minimal surface architectures. J Mech Behav Biomed Mater 62:481–494

38. Abueidda DW et al (2017) Mechanical properties of 3D printed polymeric cellular materials with triply periodic minimal surface architectures. Mater Des 122:255–267

39. Giannitelli SM et al (2014) Current trends in the design of scaffolds for computer-aided tissue engineering. Acta Biomater 10(2):580–594

40. Al-Ketan O et al (2018) Microarchitected stretching-dominated mechanical metamaterials with minimal surface topologies. Adv Eng Mater 20(9):1800029

41. Zhang L et al (2018) Energy absorption characteristics of metallic triply periodic minimal surface sheet structures under compressive loading. Addit Manuf 23:505–515

42. Yu S, Sun J, Bai J (2019) Investigation of functionally graded TPMS structures fabricated by additive manufacturing. Mater Des 182:108021

43. Yoo D (2012) New paradigms in internal architecture design and freeform fabrication of tissue engineering porous scaffolds. Medical eng phys 34(6):762–776

44. Maskery I et al (2018) Effective design and simulation of surface-based lattice structures featuring volume fraction and cell type grading. Mater Des 155:220–232

45. FEPshop. Phrozen resin ABS like gray [cited 2021 16/6/2021]. https://www.fepshop.com/shop/uv-resin/phrozen-uv-resin/phrozen-resin-abs-like-gray-5kg/

46. Hwangbo NK et al (2021) Effects of the washing time and washing solution on the biocompatibility and mechanical properties of 3D printed dental resin materials. Polymers 13(24):4410

47. Scherer MD, et al. (2022) Influence of postprocessing rinsing solutions and duration on flexural strength of aged and nonaged additively manufactured interim dental material. The Journal of Prosthetic Dentistry

48. ASTM D695 (2016) Standard test method for compressive properties of rigid plastics. ASTM International Journal of Impact Engineering

49. Yang L et al (2020) An investigation into the effect of gradients on the manufacturing fidelity of triply periodic minimal surface structures with graded density fabricated by selective laser melting. J Mater Process Technol 275:116367

50. Xiao L, Song W (2018) Additively-manufactured functionally graded Ti–6Al–4V lattice structures with high strength under static and dynamic loading: experiments. Int J Impact Eng 111:255–272

51. Al-Ketan O, Al-Rub RKA, Rowshan R (2018) The effect of architecture on the mechanical properties of cellular structures based on the IWP minimal surface. J Mater Res 33(3):343–359

52. Al-Ketan O, Rowshan R, Abu Al-Rub RK (2018) Topology-mechanical property relationship of 3D printed strut, skeletal, and sheet based periodic metallic cellular materials. Addit Manuf 19:167–183

53. Abueidda DW et al (2019) Mechanical properties of 3D printed polymeric Gyroid cellular structures: experimental and finite element study. Mater Des 165:107597

54. Al-Ketan O, Abu Al-Rub RK, Rowshan R (2018) The effect of architecture on the mechanical properties of cellular structures based on the IWP minimal surface. J Mater Res 33(3):343–359